Robotica: (2020) volume 38, pp. 2060–2079. © Cambridge University Press 2020
doi:10.1017/S0263574719001826

Modeling and Analysis of the Multiple Dynamic Coupling Effects of a Dual-arm Space Robotic System

Jianqing Peng†,‡, Wenfu Xu†,‡*, Zhonghua Hu†,‡, Bin Liang§ and Aiguo Wu†,‡

†*The School of Mechanical Engineering and Automation, Harbin Institute of Technology, Shenzhen, 518055, China*
‡*State Key Laboratory of Robotics and System, Harbin Institute of Technology, Harbin 150001, China. Emails: pjqxs@163.com, hitsz_hzh@163.com, ag.wu@163.com*
§*Department of Automation, School of Information Science and Technology, Tsinghua University, Beijing 100084, China. Email: bliang@mail.tsinghua.edu.cn*

(Accepted 14 December, 2019. First published online: January 16, 2020)

SUMMARY
A dual-arm space robot has large potentials in on-orbit servicing. However, there exist multiple dynamic coupling effects between the two arms, each arm, and the base, bringing great challenges to the trajectory planning and dynamic control of the dual-arm space robotic system. In this paper, we propose a dynamic coupling modeling and analysis method for a dual-arm space robot. Firstly, according to the conservation principle of the linear and angular momentum, the dynamic coupling between the base and each manipulator is deduced. The dynamic coupling factor is then defined to evaluate the dynamic coupling degree. Secondly, the dynamic coupling equations between the two arms, each arm, and the base are deduced, respectively. The dynamic coupling factor is suitable not only for single-arm space robots but also for multi-arm space robot systems. Finally, the multiple coupling effects of the dual-arm space robotic system are analyzed in detail through typical cases. Simulation results verified the proposed method.

KEYWORDS: Dual-arm space robot; On-orbit servicing; Trajectory planning; Dynamic coupling factor; Multiple dynamic coupling effects.

1. Introduction

With the deepening of space exploration, space debris is also increasing day by day.[1–3] How to guarantee the normal operation of on-orbit spacecraft has become a hot research topic among the international community.[4–6]

The on-orbital servicing technologies based on space robots are playing important roles in spacecraft repairing and orbital debris removal. Huang *et al*.[7] designed the dexterous tethered space robot for geostationary orbit debris removal, and the semi-physical experiments verified the feasibility of the system. Zhang *et al*.[8] studied an appropriate initial condition for tethered space net robot (TSNR) based on four releasing characters. Moreover, an enlightened second-order sliding mode control scheme was proposed for the stability control of TSNR. Nanos and Papadopoulos *et al*.[9,10] proposed a novel path planning method allowing the end-effector to follow a desired path avoiding any dynamic singularities, the method can be applied to any desired end-effector trajectories. Pre-contact trajectory planning technology plays a very important role in on-orbit service. The main

* Corresponding author. E-mail: wfxu@hit.edu.cn

research of this paper is the trajectory planning for target pre-capturing. For example, how to reduce the disturbance of the base by designing the configuration of the manipulator and rationally distributing the mass inertia? How to minimize the disturbance of the base by planning the motion of the manipulator? The study of these issues will be of great significance for space robots to perform capture operations.

For a free-floating space robot system, the movement of the end-effector causes disturbance to the base, which is mainly reflected in the changes in the position and attitude of the base centroid. This change in turn affects the pose of the end-effector; there is a dynamic coupling between the manipulator and the base.[11,12] Based on the particle swarm optimization algorithm, Xu *et al.*[13] introduced a method to plan the Cartesian point-to-point path of the end-effector; meanwhile, the base attitude can be controlled. Xu *et al.*[14] also designed a unified multi-domain modeling and simulation system. To effectively study the dynamic coupling theory, Xu *et al*. derived a dynamic coupling model for a space robotic system[15] and underactuated manipulators.[16] They also proposed the coupling factor to illustrate the motion and force dependencies, and represent the degree of the dynamic coupling.

As single-arm space robots cannot perform complex and ingenious operations, the dual-arm space robots[17] are becoming more and more flexible and reliable and are becoming the mainstay of future on-orbit services. Papadopoulos *et al.*[18] and Ali *et al*.[19] proposed the two model-based and one-transposed Jacobian control algorithms; this method implements coordinated tracking control of the manipulators and the spacecraft. Hafez *et al.*[20,21] proposed a visual servoing controller based on a task redundancy approach for a dual-arm space robot, this method achieves the coordination of the end-effector's motion with the spacecraft attitude. Wang *et al.*[22] also presented the coordinated motion planning method of a dual-arm space robot. In addition, Peng *et al.*[23] proposed a dual-arm coordinated capturing method based on efficient parameters estimation. But all consider simple situations. In the process of target capturing, it is necessary to avoid or minimize the influence of the dynamic coupling; at the same time, in the process of attitude adjustment, we can use this kind of dynamic coupling to perform rapid attitude adjustment.

This approach studies the dynamic modeling and coupling characteristics of a dual-arm space robot system and provides a theoretical basis for a dual-arm coordination trajectory planning. The coupling of the dual-arm space robot system is mainly divided into two types: one is the dynamic coupling between the two arms; the other is the dynamic coupling between the base and the two arms. Based on the conservation of momentum, we completely analyze the coupling between the base and the manipulator and decompose the dynamic coupling relationship into the position and velocity level. The comparison of the coupled space and the working space is then derived. Furthermore, the multiple dynamic coupling effects of a dual-arm space robotic system are modeled and analyzed.

The remainder of this paper is organized as follows. In Section 2, the kinematic equation of a dual-arm space robot is established. Section 3 introduces the dynamic coupling decomposition concept. Section 4 derives the dynamic coupling of the dual-arm space robot and analyzes the corresponding coupling factor. Numerical simulation is discussed in Section 5. The last section presents the summary and conclusions.

2. Modeling of a Dual-arm Space Robotic System

A dual-arm space robotic system is composed of a robot base, an n_a-degrees of freedom (DOF) serial manipulator (called Arm-a), and an n_b-DOF serial manipulator (called Arm-b). The model is shown in Fig. 1. The symbols are defined as follows: B_0 denotes the satellite main body, B_i^k ($i = 1, \cdots, n_k$; $k = a$ or b; hereafter the same) denotes the i^{th} link of Arm-k, and J_i^k is the i^{th} joint of Arm-k. Joint J_i^k connects B_i^k and B_{i-1}^k, where $B_0^k = B_0$; C_0 and C_i^k are, respectively, the center of mass (CM) of B_0 and B_i^k; $\boldsymbol{r}_0, \boldsymbol{r}_i^k$, and $\boldsymbol{r}_g \in \boldsymbol{R}^3$ are the position vector of C_0, C_i^k, and the system's CM; $\boldsymbol{p}_e^k \in \boldsymbol{R}^3$ is the position vector of Arm-k's end-effector; $\boldsymbol{v}_e^k, \boldsymbol{\omega}_e^k \in \boldsymbol{R}^3$ are the linear and angular velocities of Arm-k's end-effector, and they can be combined as $\dot{\boldsymbol{x}}_e^k = \left[\left(\boldsymbol{v}_e^k\right)^{\mathrm{T}}, \left(\boldsymbol{\omega}_e^k\right)^{\mathrm{T}}\right]^{\mathrm{T}} \in \boldsymbol{R}^6$; $\boldsymbol{v}_0, \boldsymbol{\omega}_0 \in \boldsymbol{R}^3$ are the linear and angular velocities of B_0, which can be combined as $\dot{\boldsymbol{x}}_0 = \left[\boldsymbol{v}_0^{\mathrm{T}}, \boldsymbol{\omega}_0^{\mathrm{T}}\right]^{\mathrm{T}} \in \boldsymbol{R}^6$; m_0 *and* m_i^k are the mass of B_0 and B_i^k; the total mass of the system is $M = m_0 + \sum_{k=1}^{N}\left(\sum_{i=1}^{n_k} m_i^{(k)}\right)$; $\boldsymbol{\Theta}^k = \left[\theta_1, \cdots, \theta_{n_k}\right]^{\mathrm{T}}$ is the vector composed of the joint variables of Arm-k; $\sum_I$, $\sum_0$ are the inertia frame and the base fixed frame, respectively; $\sum_{Ek}$ the Arm-k's end-effector frame; $\sum_i^k (i = 1, \cdots, n_k)$ is the

https://doi.org/10.1017/S0263574719001826 Published online by Cambridge University Press

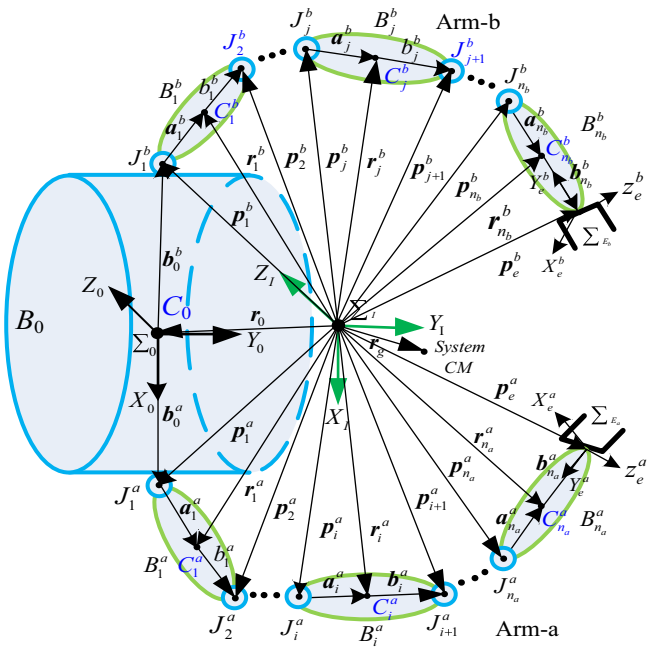

Fig. 1. A general model of a dual-arm space robot system.

body fixed frame of B_i^k; ${}^iA_j \in \boldsymbol{R}^{3\times3}$ is the rotation matrix of $\sum_j^k$ with respect to $\sum_i^k$; ${}^i\boldsymbol{I}_i \in \boldsymbol{R}^{3\times3}$ $(i = 1, \cdots, n_k)$ is the inertia matrix of B_i^k with respect to its CM; $\boldsymbol{k}_i^k \in \boldsymbol{R}^{3\times3}(i = 1, \cdots, n)$ is the unit vector representing the rotation direction of J_i^k; $\boldsymbol{p}_i^k \in \boldsymbol{R}^3(i = 1, \cdots, n_k)$ is the position vector of J_i^k; $\boldsymbol{a}_i^k, \boldsymbol{b}_i^k, \boldsymbol{l}_i^k = \boldsymbol{a}_i^k + \boldsymbol{b}_i^k \in \boldsymbol{R}^3(i = 1, \cdots, n_k)$ are the position vectors from J_i^k to C_i^k and C_{i+1}^k to J_{i+1}^k, respectively; $\boldsymbol{v}_i^k, \boldsymbol{\omega}_i^k \in \boldsymbol{R}^3$ are the linear and angular velocities of B_i^k, respectively.

According to Fig. 1, the position vector of B_i^k's centroid is determined as follows:

$$\boldsymbol{r}_i^k = \boldsymbol{r}_0 + \boldsymbol{b}_0^k + \sum_{j=1}^{i-1}\left(\boldsymbol{a}_j^k + \boldsymbol{b}_j^k\right) + \boldsymbol{a}_i^k \tag{1}$$

As external forces and torques acting on the system are negligible, the CM of the base is determined by:

$$\boldsymbol{r}_0 = \boldsymbol{r}_g - \left(\tilde{\boldsymbol{b}}_0^k + \sum_{i=1}^{n_k-1}\left(\tilde{\boldsymbol{a}}_i^k + \tilde{\boldsymbol{b}}_i^k\right) + \tilde{\boldsymbol{a}}_n^k\right) \tag{2}$$

where $\tilde{\boldsymbol{a}}_i^k = \frac{\sum_{q=i}^{n_k} m_q}{M}\boldsymbol{a}_i^k$ $(i = 1, 2, \cdots, n_k)$, $\tilde{\boldsymbol{b}}_i^k = \frac{\sum_{q=i+1}^{n_k} m_q}{M}\boldsymbol{b}_i^k$ $(i = 0, 1, \cdots, n_k - 1)$.

Thus, the position vector of the end-effector can be described as:

$$\boldsymbol{p}_e^k = \boldsymbol{r}_g + \hat{\boldsymbol{b}}_0^k + \sum_{j=1}^{n_k}\left(\hat{\boldsymbol{a}}_j^k + \hat{\boldsymbol{b}}_j^k\right) \tag{3}$$

where $\hat{\boldsymbol{a}}_i^k = \frac{\sum_{q=0}^{i-1} m_q}{M}\boldsymbol{a}_i^k$, $\hat{\boldsymbol{b}}_i^k = \frac{\sum_{q=0}^{i} m_q}{M}\boldsymbol{b}_i^k$ $(i = 1, 2, \cdots, n_k)$.

The general kinematics equation of Arm-k $(k = a, b)$ is as follows:[24,25]

$$\begin{bmatrix}\dot{\boldsymbol{x}}_e^a \\ \dot{\boldsymbol{x}}_e^b\end{bmatrix} = \begin{bmatrix}\boldsymbol{J}_b^a \\ \boldsymbol{J}_b^b\end{bmatrix}\dot{\boldsymbol{x}}_0 + \begin{bmatrix}\boldsymbol{J}_m^a & \\ & \boldsymbol{J}_m^b\end{bmatrix}\begin{bmatrix}\dot{\boldsymbol{\Theta}}^a \\ \dot{\boldsymbol{\Theta}}^b\end{bmatrix} \tag{4}$$

https://doi.org/10.1017/S0263574719001826 Published online by Cambridge University Press

where $\boldsymbol{J}_{\mathrm{b}}^{k}=\begin{pmatrix}\boldsymbol{E}_3 & -\check{\boldsymbol{p}}_{0\mathrm{e}}^{k}\\ \boldsymbol{O}_3 & \boldsymbol{E}_3\end{pmatrix}\in\boldsymbol{R}^{6\times6}$, $\boldsymbol{p}_{0\mathrm{e}}^{k}=\boldsymbol{p}_{\mathrm{e}}^{k}-\boldsymbol{r}_0$, $\boldsymbol{J}_{\mathrm{m}}^{k}=\begin{bmatrix}\boldsymbol{k}_1^k\times\left(\boldsymbol{p}_{\mathrm{e}}^{k}-\boldsymbol{p}_1^k\right)&\ldots&\boldsymbol{k}_n^k\times\left(\boldsymbol{p}_{\mathrm{e}}^{k}-\boldsymbol{p}_n^k\right)\\ \boldsymbol{k}_1^k&\ldots&\boldsymbol{k}_n^k\end{bmatrix}\in\mathbf{R}^{6\times n}$, $\check{\boldsymbol{p}}_{0\mathrm{e}}^{k}$ is the skew-symmetric matrix determined by $\boldsymbol{p}_{0e}^{k}$, $\boldsymbol{E}_3$ and $\boldsymbol{O}_3$ represent the identity and zeros matrixes of 3 rows and 3 columns, respectively.

For a free-floating space robot, the values of linear and angular momentum are constant; in order to simplify the expression, here we think that the initial momentum of the system is zero, then:

$$\begin{pmatrix}\boldsymbol{ME} & \boldsymbol{M}\check{\boldsymbol{r}}_{0g}^{T}\\ \boldsymbol{M}\check{\boldsymbol{r}}_{0g} & \boldsymbol{H}_w\end{pmatrix}\dot{\boldsymbol{x}}_0+\begin{bmatrix}\boldsymbol{J}_{Tw}^{a}\\ \boldsymbol{H}_{w\phi}^{a}\end{bmatrix}\dot{\boldsymbol{\Theta}}^{a}+\begin{bmatrix}\boldsymbol{J}_{Tw}^{b}\\ \boldsymbol{H}_{w\phi}^{b}\end{bmatrix}\dot{\boldsymbol{\Theta}}^{b}=0 \tag{5}$$

where matrix $\boldsymbol{E}$ is the identity matrix, $\boldsymbol{H}_w=\boldsymbol{I}_0+\sum_{k=1}^{N}\left(\sum_{i=1}^{n_k}\left(\boldsymbol{I}_i^k+m_i^k\check{\boldsymbol{r}}_i^k\left(\check{\boldsymbol{r}}_{0i}^{k}\right)^{\mathrm{T}}\right)\right)$, $\boldsymbol{r}_{0i}^{k}=\boldsymbol{r}_i^k-\boldsymbol{r}_0$, $\boldsymbol{J}_{Tw}^{k}=\sum_{i=1}^{n_k}\left(m_i^k\boldsymbol{J}_{Ti}^{k}\right)\in\mathbf{R}^{3\times n_k}$, $\boldsymbol{H}_{\omega\phi}^{k}=\sum_{i=1}^{n_k}\left(\boldsymbol{I}_i^k\boldsymbol{J}_{Ri}^{k}+m_i^k\check{\boldsymbol{r}}_i^k\boldsymbol{J}_{Ti}^{k}\right)$, $\boldsymbol{J}_{Ri}^{k}=\begin{cases}\left[\boldsymbol{z}_1^k,\cdots,\boldsymbol{z}_i^k,0,\cdots,0\right], & \text{rotational joint}\\ \left[0,\cdots,0,0,\cdots,0\right], & \text{translational joint}\end{cases}$,

$\boldsymbol{r}_{0g}=\boldsymbol{r}_g-\boldsymbol{r}_0$, $\boldsymbol{J}_{Ti}^{k}=\begin{cases}\left[\boldsymbol{z}_1^k\times\left(\boldsymbol{r}_i^k-\boldsymbol{p}_1^k\right),\cdots,\boldsymbol{z}_i^k\times\left(\boldsymbol{r}_i^k-\boldsymbol{p}_i^k\right),0,\cdots,0\right]\in\mathbf{R}^{3\times n_k}, & \text{rotational joint}\\ \left[\boldsymbol{z}_1^k,\cdots,\boldsymbol{z}_i^k,0,\cdots,0\right]\in\mathbf{R}^{3\times n_k}, & \text{translational joint}\end{cases}$.

By combining (4) with (5), we obtain

$$\dot{\boldsymbol{x}}_e^{ab}=\begin{bmatrix}\dot{\boldsymbol{x}}_e^{a}\\ \dot{\boldsymbol{x}}_e^{b}\end{bmatrix}=\begin{bmatrix}\boldsymbol{J}_{aa}^{*}&\boldsymbol{J}_{ab}^{*}\\ \boldsymbol{J}_{ba}^{*}&\boldsymbol{J}_{bb}^{*}\end{bmatrix}\begin{bmatrix}\dot{\boldsymbol{\Theta}}^{a}\\ \dot{\boldsymbol{\Theta}}^{b}\end{bmatrix}=\boldsymbol{J}_g\begin{bmatrix}\dot{\boldsymbol{\Theta}}^{a}\\ \dot{\boldsymbol{\Theta}}^{b}\end{bmatrix} \tag{6}$$

where $\boldsymbol{J}_g=\begin{bmatrix}\boldsymbol{J}_{aa}^{*}&\boldsymbol{J}_{ab}^{*}\\ \boldsymbol{J}_{ba}^{*}&\boldsymbol{J}_{bb}^{*}\end{bmatrix}\in\boldsymbol{R}^{12\times(n_a+n_b)}$, $\boldsymbol{J}_{aa}^{*}=-\boldsymbol{J}_b^a\boldsymbol{H}_0^{-1}\boldsymbol{H}_{0m}^{a}+\boldsymbol{J}_m^a$, $\boldsymbol{J}_{ab}^{*}=-\boldsymbol{J}_b^a\boldsymbol{H}_0^{-1}\boldsymbol{H}_{0m}^{a}$, $\boldsymbol{J}_{ba}^{*}=-\boldsymbol{J}_b^b\boldsymbol{H}_0^{-1}\boldsymbol{H}_{0m}^{a}$, $\boldsymbol{J}_{bb}^{*}=-\boldsymbol{J}_b^b\boldsymbol{H}_0^{-1}\boldsymbol{H}_{0m}^{a}+\boldsymbol{J}_m^b$, $\boldsymbol{H}_0=\begin{pmatrix}\boldsymbol{ME}_3 & \boldsymbol{M}\check{\boldsymbol{r}}_{0g}^{T}\\ \boldsymbol{M}\check{\boldsymbol{r}}_{0g} & \boldsymbol{H}_w\end{pmatrix}\in\boldsymbol{R}^{6\times6}$, $\boldsymbol{H}_{0m}^{k}=\begin{bmatrix}\boldsymbol{J}_{Tw}^{k}\\ \boldsymbol{H}_{w\phi}^{k}\end{bmatrix}\in\boldsymbol{R}^{6\times n_k}$.

From (5), the velocity of the base centroid is determined by:

$$\dot{\boldsymbol{x}}_0=\boldsymbol{J}_{0m}^{a}\dot{\boldsymbol{\Theta}}^{a}+\boldsymbol{J}_{0m}^{b}\dot{\boldsymbol{\Theta}}^{b}=\begin{bmatrix}\boldsymbol{J}_{0m}^{a}&\boldsymbol{J}_{0m}^{b}\end{bmatrix}\begin{bmatrix}\dot{\boldsymbol{\Theta}}^{a}\\ \dot{\boldsymbol{\Theta}}^{b}\end{bmatrix}=\boldsymbol{J}_{0m}\begin{bmatrix}\dot{\boldsymbol{\Theta}}^{a}\\ \dot{\boldsymbol{\Theta}}^{b}\end{bmatrix} \tag{7}$$

where $\boldsymbol{J}_{0m}^{k}=\begin{bmatrix}\boldsymbol{J}_{0m\_v}^{k}\\ \boldsymbol{J}_{0m\_\omega}^{k}\end{bmatrix}=\begin{bmatrix}-\check{\boldsymbol{r}}_{0g}\boldsymbol{H}_0^{-1}\boldsymbol{H}_{0m}^{k}-\frac{\boldsymbol{J}_{Tw}^{k}}{M}\\ -\boldsymbol{H}_0^{-1}\boldsymbol{H}_{0m}^{k}\end{bmatrix}$, $\boldsymbol{J}_{0m}=\left[\boldsymbol{J}_{0m}^{a},\boldsymbol{J}_{0m}^{b}\right]$.

Combining (7) with (6) yields

$$\dot{\boldsymbol{x}}_0=\boldsymbol{J}_{0m}\boldsymbol{J}_g^{-1}\cdot\left[\dot{\boldsymbol{x}}_e^{a},\dot{\boldsymbol{x}}_e^{b}\right]^{\mathrm{T}} \tag{8}$$

3. Dynamic Coupling Decomposition Concept

Generally speaking, the concept of dynamic coupling was used to analyze the influence of the movement of the end-effector to the movement of the base for a single-arm space robot, which is described by the L_2 norm ratio of the generalized velocities of the end-effector to the generalized velocities of the base centroid. The disadvantage of it is the singular configuration is various and the computational efficiency is low. The single-arm base-to-end dynamics coupling model can be further extended to the dual-arm space robot system. As shown in Fig. 2, the dynamic coupling characteristics of the dual-arm space robot are extremely complex and are mainly divided into the following two categories:

(a) Dynamic coupling between two arms;
(b) Dynamic coupling between dual-arm and the base.

Since the linear momentum and angular momentum equations have their own unique characteristics, they can be solved independently by different methods, which can avoid the traditional

https://doi.org/10.1017/S0263574719001826 Published online by Cambridge University Press

Table I. The comparison of VM and BCVM.

Name	**VM**[26]	**BCVM**[27]
End-effector or	$\hat{\boldsymbol{p}}_{\mathrm{e},k}^{\mathrm{VM}} = \boldsymbol{r}_g + \hat{\boldsymbol{b}}_0^k + \sum_{i=1}^{n_k} \left(\hat{\boldsymbol{a}}_i^k + \hat{\boldsymbol{b}}_i^k\right)$	$\tilde{\boldsymbol{P}}_{\mathrm{e},k}^{\mathrm{BCVM}} = \tilde{\boldsymbol{b}}_0^k + \sum_{i=1}^{n_k-1} \left(\tilde{\boldsymbol{a}}_i^k + \tilde{\boldsymbol{b}}_i^k\right) + \tilde{\boldsymbol{a}}_n^k$
Virtual link	$\begin{cases} \hat{\boldsymbol{b}}_i^k = \frac{\sum_{q=0}^{i} m_q}{M} \boldsymbol{b}_i^k \\ \hat{\boldsymbol{a}}_i^k = \frac{\sum_{q=0}^{i-1} m_q}{M} \boldsymbol{a}_i^k \end{cases} (i = 1, \cdots, n_k)$	$\begin{cases} \tilde{\boldsymbol{a}}_i^k = \frac{\sum_{q=i}^{n_k} m_q}{M} \boldsymbol{a}_i^k \ (i = 1, \cdots, n_k) \\ \tilde{\boldsymbol{b}}_i^k = \frac{\sum_{q=i+1}^{n_k} m_q}{M} \boldsymbol{b}_i^k \ (i = 0, \cdots, n_k - 1) \end{cases}$

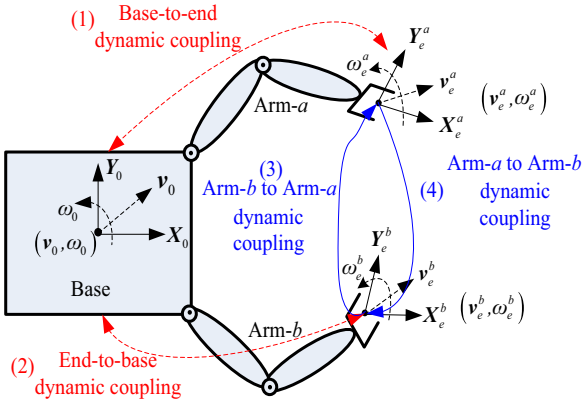

Fig. 2. Dynamic coupling for a dual-arm space robot.

redundant solution. Because the momentum equation is integrable, it is a conservation constraint while the angular momentum equation is not integrable. Based on the characteristics of this constraint, the kinematics equations at the position and velocity level can be split, and the corresponding equations can be solved independently. According to this decomposition idea, the dynamic coupling of the space robot can be divided into two subsystems: one is the position-level dynamic coupling between the maximum reachable working space (RWS) and the base centroid coupling space; the other is the velocity-level dynamic coupling between the end-effector's velocity and the base angular velocity. According to (3) and (2), the vector directions of $\hat{\boldsymbol{a}}_i^k$, $\hat{\boldsymbol{b}}_i^k$, $\tilde{\boldsymbol{a}}_i^k$, $\tilde{\boldsymbol{b}}_i^k$, and $\boldsymbol{a}_i^k$, $\boldsymbol{b}_i^k$ are the same, and the corresponding proportional constants are different in length, which becomes a "*virtual link vector*." Meanwhile, the centroid of the system is defined as virtual ground, as shown in Table I.

The pose mapping relationship between the base centroid and the end-effector is shown in Fig. 3. In Fig. 3, $\tilde{\boldsymbol{P}}_{e,k}^{BCVM}$, *kine* $\left(\boldsymbol{\Theta}^k\right)$, and *ikine* $\left(\boldsymbol{P}_e^k\right)$ represent the end-effector of base centroid virtual manipulator (BCVM), the forward kinematic equation, and the inverse kinematic equation, respectively. The maximum RWS[26] of a virtual manipulator (VM) is a ball whose center is the system centroid, and the maximum reachable coupling space (RCS)[27] of a BCVM is also a ball whose center is the system centroid; the coupling space radius $\mathrm{R_{RCS}}$ and the working space radius $\mathrm{R_{RWS}}$ are:

$$\begin{cases} R_{\mathrm{RCS}}^k = \max\limits_{\theta_0^k, \theta_i^k \in [-\pi, \pi]} \left(\left\| {}^0\tilde{\boldsymbol{b}}_0^k + \sum_{i=1}^{n_k} {}^0\boldsymbol{A}_i^k \left({}^i\tilde{\boldsymbol{a}}_i^k + {}^i\tilde{\boldsymbol{b}}_i^k \right) \right\| \right) \\ R_{\mathrm{RWS}}^k = \max\limits_{\theta_0^k, \theta_i^k \in [-\pi, \pi]} \left(\left\| {}^0\hat{\boldsymbol{b}}_0^k + \sum_{i=1}^{n_k} {}^0\boldsymbol{A}_i^k \left({}^i\hat{\boldsymbol{a}}_i^k + {}^i\hat{\boldsymbol{b}}_i^k \right) \right\| \right) \end{cases} \tag{9}$$

where ${}^0\boldsymbol{A}_i^k$ represents the attitude transformation matrix from the original coordinate system to the i^{th} coordinate system corresponding to Arm-k.

As shown in Fig. 4, a planar 2-DoF robot is used as an example to illustrate the workspace of the VM and BCVM.[27]

https://doi.org/10.1017/S0263574719001826 Published online by Cambridge University Press

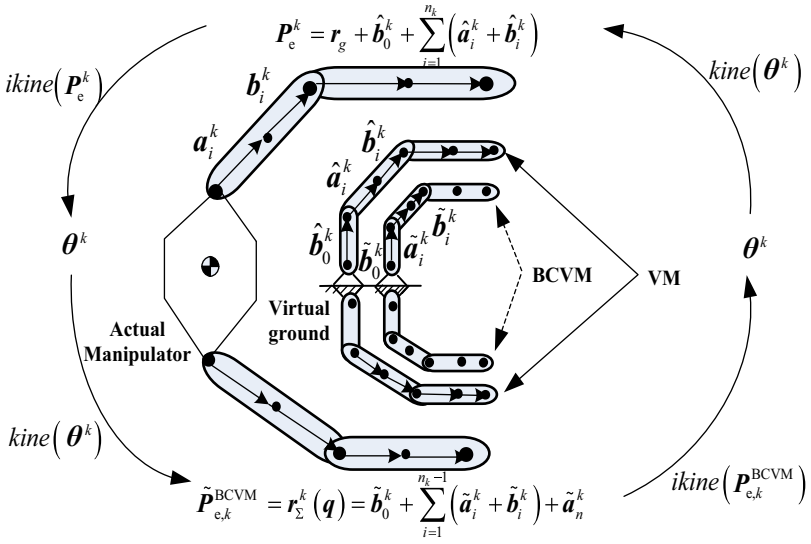

Fig. 3. The coupling diagram in position level.

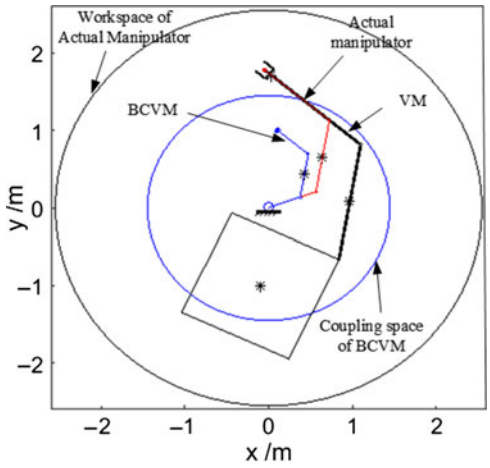

Fig. 4. Comparison of the coupled space and the working space.

4. Dynamic Coupling of a Dual-arm Space Robotic System

Theorem 1. *Consider a non-zero matrix* $\boldsymbol{A}$*, and* $\boldsymbol{A}$ *is an nth-order square matrix. If the eigenvalues of the matrix* $\boldsymbol{A}$ *are* $\lambda_1, \cdots, \lambda_n$ $(0 \le \lambda_1 \le \cdots \le \lambda_n)$*, and the corresponding eigenvectors are* $\boldsymbol{p}_1, \cdots, \boldsymbol{p}_n$*, then for any non-zero vector* $\boldsymbol{x} \in \boldsymbol{R}^{n\times 1}$*, the parameter* $\kappa = \frac{\boldsymbol{x}^{\mathrm{T}}\boldsymbol{A}\boldsymbol{x}}{\boldsymbol{x}^{\mathrm{T}}\boldsymbol{x}}$ *is bounded between* λ_1 *and* λ_n*.*

Proof. According to the above assumption, the vector $\boldsymbol{x}$ can be expressed as:

$$\boldsymbol{x} = c_1\boldsymbol{p}_1 + \cdots + c_n\boldsymbol{p}_n \tag{10}$$

where c_i $(i = 1, \cdots, n)$ represents the coefficient of $\boldsymbol{p}_i$, and $c_1^2 + \cdots + c_n^2 \neq 0$.

Then, the above parameter can be rewritten as:

$$\kappa = \frac{c_1^2\lambda_1 + \cdots + c_n^2\lambda_n}{c_1^2 + \cdots + c_n^2} = k_1\lambda_1 + \cdots + k_n\lambda_n \tag{11}$$

where $k_i = \frac{c_i^2}{c_1^2+\cdots+c_n^2}(i = 1, \cdots, n)$, $\sum_{i=1}^{n} k_i = 1$.

According to (11), we can conclude that κ satisfies the following inequality:

$$\lambda_1(\boldsymbol{A}) \le \kappa \le \lambda_n(\boldsymbol{A}) \tag{12}$$

https://doi.org/10.1017/S0263574719001826 Published online by Cambridge University Press

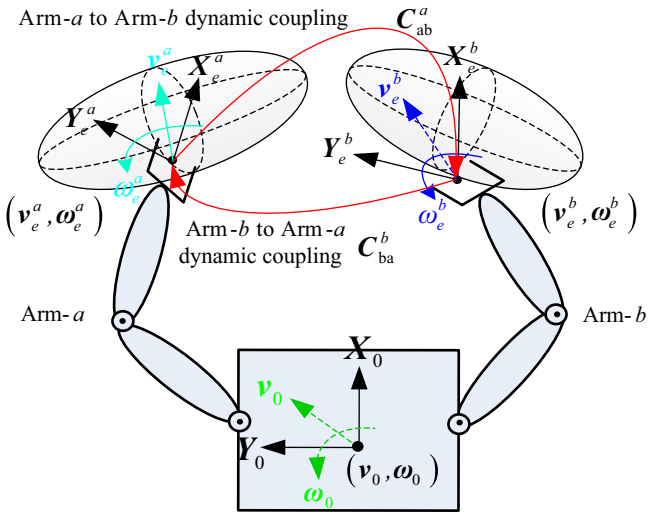

Fig. 5. The dynamic coupling diagram of Arm-*a* to Arm-*b*.

4.1. Dynamic coupling between two arms

Based on the kinematical modeling of the dual-arm space robot derived above, the ratio between the velocity of Arm-*a*'s end-effector and the velocity of Arm-*b*'s end-effector is determined by:

$$\sigma_{\mathrm{ab}}(\dot{\boldsymbol{x}}_e^a) = \frac{\left\|\dot{\boldsymbol{x}}_e^b\right\|_2}{\left\|\dot{\boldsymbol{x}}_e^a\right\|_2} = \frac{\left\langle \boldsymbol{C}_{\mathrm{ab}}^a \dot{\boldsymbol{x}}_e^a, \boldsymbol{C}_{\mathrm{ab}}^a \dot{\boldsymbol{x}}_e^a \right\rangle^{1/2}}{\left\langle \dot{\boldsymbol{x}}_e^a, \dot{\boldsymbol{x}}_e^a \right\rangle^{1/2}} = \sqrt{\frac{\left(\dot{\boldsymbol{x}}_e^a\right)^{\mathrm{T}} \boldsymbol{A}_{\mathrm{ab}}^a \dot{\boldsymbol{x}}_e^a}{\left(\dot{\boldsymbol{x}}_e^a\right)^{\mathrm{T}} \dot{\boldsymbol{x}}_e^a}} \tag{13}$$

where $\boldsymbol{C}_{\mathrm{ab}}^a = \left[\boldsymbol{J}_{ba}^* \boldsymbol{J}_{bb}^*\right]\left[\boldsymbol{J}_{aa}^* \boldsymbol{J}_{ab}^*\right]^{\#}$, $\boldsymbol{A}_{\mathrm{ab}}^a = \left(\boldsymbol{C}_{\mathrm{ab}}^a\right)^{\mathrm{T}} \boldsymbol{C}_{\mathrm{ab}}^a$, and the symbol $[\cdot]^{\#}$ denotes the generalized inverse matrix.

Therefore, the dynamic coupling between Arm-*a* and Arm-*b* is shown in Fig. 5. Here, $\boldsymbol{C}_{\mathrm{ab}}^a$ represents the variation extent of Arm-*b* generated by Arm-*a* motion. Assuming that $\mu_1, \cdots, \mu_n$ $(0 \le \mu_1 \le \cdots \le \mu_n)$ are the eigenvalues of the matrix $\boldsymbol{A}_{ab}^a$, and $\boldsymbol{\gamma}_1, \cdots, \boldsymbol{\gamma}_n$ are the corresponding orthonormal eigenvectors, the dynamic coupling factor from Arm-*a* to Arm-*b* satisfies the following inequality:

$$\sqrt{\mu_1\left(\boldsymbol{A}_{ab}^a\right)} \le \sigma_{ab} \le \sqrt{\mu_n\left(\boldsymbol{A}_{ab}^a\right)} \tag{14}$$

The coupling matrix $\boldsymbol{C}_{\mathrm{ab}}^a$ is related to the mass characteristics of the base and the manipulator, the joint angle of the manipulator, and the attitude of the base. Through analysis, the following conclusions can be drawn:

(1) If the mass characteristics of Arm-*b* are much larger than those of Arm-*a*, that is, the influence of the motion from Arm-*a* to Arm-*b* is small, the dynamic coupling is negligible; conversely, the influence of the motion from Arm-*b* to the base cannot be ignored, and the dynamic coupling must be considered.
(2) By reasonably designing the installation position of the manipulator, the distribution of singular values of the matrix $\boldsymbol{A}_{ab}^a$ can be changed, thereby effectively reducing the dynamic coupling characteristics.
(3) By rationally planning the motion trajectory of the robot, the distribution of the singular values of the matrix $\boldsymbol{A}_{ab}^a$ can also be changed, thereby effectively reducing the dynamic coupling characteristics.

https://doi.org/10.1017/S0263574719001826 Published online by Cambridge University Press

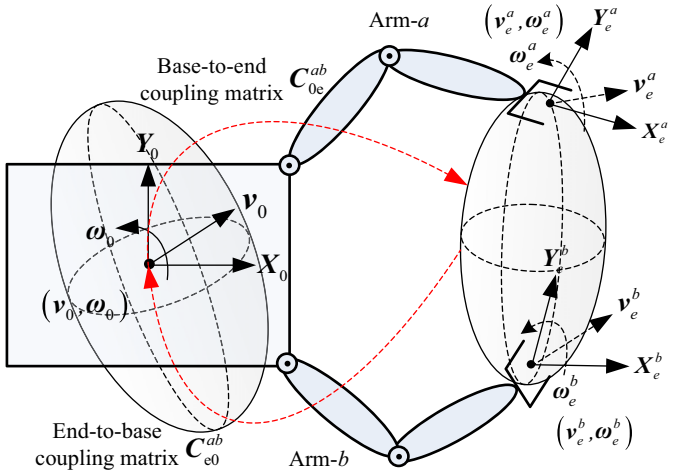

Fig. 6. The dynamic coupling diagram of end-to-base.

4.2. Dynamic coupling between the dual-arm and the base

Based on the derivation from Section 2, the coupling of the end-effector to the base can be expressed as:

$$\sigma_{e0}^{ab}(\dot{\boldsymbol{x}}_e^{ab}) = \frac{\|\dot{\boldsymbol{x}}_0\|}{\|\dot{\boldsymbol{x}}_e^{ab}\|} = \frac{\left\langle \boldsymbol{C}_{e0}^{ab}\,\dot{\boldsymbol{x}}_e^{ab},\, \boldsymbol{C}_{e0}^{ab}\,\dot{\boldsymbol{x}}_e^{ab} \right\rangle^{1/2}}{\left\langle \dot{\boldsymbol{x}}_e^{ab},\, \dot{\boldsymbol{x}}_e^{ab} \right\rangle^{1/2}} = \sqrt{\frac{\left(\dot{\boldsymbol{x}}_e^{ab}\right)^{\mathrm{T}} \boldsymbol{A}_{e0}^{ab}\,\dot{\boldsymbol{x}}_e^{ab}}{\left(\dot{\boldsymbol{x}}_e^{ab}\right)^{\mathrm{T}}\,\dot{\boldsymbol{x}}_e^{ab}}} \tag{15}$$

where $\boldsymbol{C}_{e0}^{ab} = \boldsymbol{J}_{0m}\,\boldsymbol{J}_g^{-1}, \boldsymbol{A}_{e0}^{ab} = \left(\boldsymbol{C}_{e0}^{ab}\right)^{\mathrm{T}}\,\boldsymbol{C}_{e0}^{ab}$.

The coupling relationship between the end-effector's velocity and the base velocity is shown in Fig. 6. Here, $\boldsymbol{C}_{e0}^{ab}$ describes the variation degree of the base attitude caused by the given end-effector motion. Assuming that $\lambda_1, \cdots, \lambda_n$ $(0 \le \lambda_1 \le \cdots \le \lambda_n)$ are the eigenvalues of the matrix $\boldsymbol{A}_{e0}^{ab}$, and $\boldsymbol{p}_1, \cdots, \boldsymbol{p}_n$ are the corresponding orthonormal eigenvectors, the end-to-base dynamic coupling factor satisfies the following inequality:

$$\sqrt{\lambda_1\left(\boldsymbol{A}_{e0}^{ab}\right)} \le \sigma_{e0}^{ab} \le \sqrt{\lambda_n\left(\boldsymbol{A}_{e0}^{ab}\right)} \tag{16}$$

Similarly, through the above analysis, the following conclusions can be drawn:

(1) If the mass characteristics of the base are much larger than those of the manipulator, that is, the influence of the motion of the manipulator to the base is small, the dynamic coupling is negligible; conversely, the influence of the motion of the manipulator to the base cannot be ignored, and the dynamic coupling must be considered.
(2) By reasonably designing the installation position of the manipulator, the distribution of the singular values of the matrix $\boldsymbol{A}_{e0}^{ab}$ can be changed, thereby effectively reducing the dynamic coupling characteristics.
(3) By rationally planning the motion trajectory of the robot, the distribution of the singular values of the matrix $\boldsymbol{A}_{e0}^{ab}$ can also be changed, thereby effectively reducing the dynamic coupling characteristics.

5. Multiple Coupling Effects Analysis of a Practical Space Robotics System

5.1. Dynamic coupling simulation analysis

5.1.1. A dual-arm space robotic system. In order to better demonstrate the dynamic coupling characteristics between dual-arm space robot systems, we use a planar 2-DoF dual-arm space robot system as an example. Assuming that φ_a, φ_b are the rotation angles of the x-axis of the base body frame 0 to vector $\boldsymbol{b}_0^a$, $\boldsymbol{b}_0^b$, respectively, the mass property of the dual-arm robot is shown in Table II.

https://doi.org/10.1017/S0263574719001826 Published online by Cambridge University Press

Table II. The mass parameters of a planar 2-DoF dual-arm robot system.

Parameter	**Base**	$\boldsymbol{B}_{1a}$	$\boldsymbol{B}_{2a}$	$\boldsymbol{B}_{1b}$	$\boldsymbol{B}_{2b}$
Mass (kg)	400	20	20	20	20
${}^{i}\boldsymbol{a}_{i}$(m)	–	0.5	0.5	0.5	0.5
	–	0	0	0	0
${}^{i}\boldsymbol{b}_{i}$(m)	0.5 –0.5	0.5	0.5	0.5	0.5
	0.5 0.5	0	0	0	0
$\boldsymbol{I}_{i}$ (kg.m^2)	48	2.4	2.4	2.4	2.4

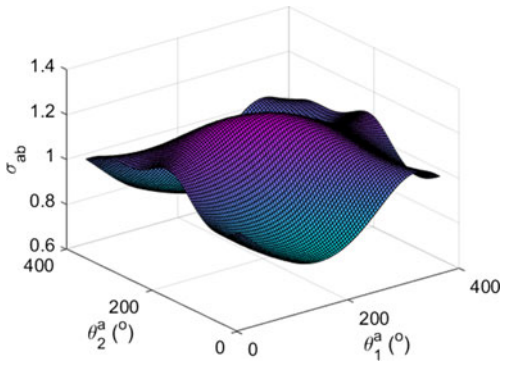

Fig. 7. The coupling map varies with the joint angle of Arm-*a* in 3D form with $m_{\mathrm{L}} = 0$.

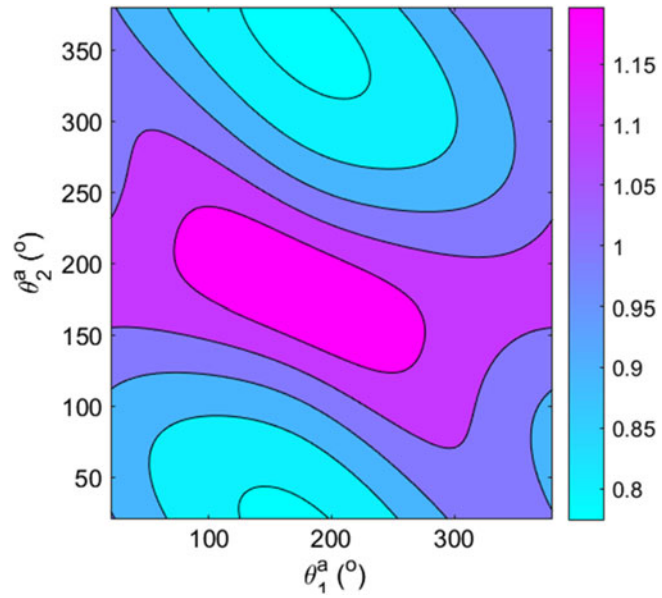

Fig. 8. The coupling map varies with the joint angle of Arm-*a* in 2D form with $m_{\mathrm{L}} = 0$.

5.1.2. Dynamic coupling between two arms. The 3D, 2D, and the contour line of the coupling factor of Arm-*a* to Arm-*b* that varies with the joint angle of Arm-*a* are shown in Figs. 7, 8, and 9, respectively. The coupling factor that varies with Arm-*b* is shown in Fig. 10, and the contour line that varies with the joint angle of Arm-*a* is shown in Fig. 11. When the payload of Arm-*a* is $m_{\mathrm{L}} = 100$ kg, the coupling factor of Arm-*a* to Arm-*b* that varies with the joint angle of Arm-*a* and Arm-*b* is shown in Figs. 11 and 12, respectively.

In addition, the dynamic coupling factor from Arm-*a* to Arm-*b* that varies with the dual-arm installation angle is shown in Fig. 13, and the corresponding contour lines are shown in Fig. 14.

https://doi.org/10.1017/S0263574719001826 Published online by Cambridge University Press

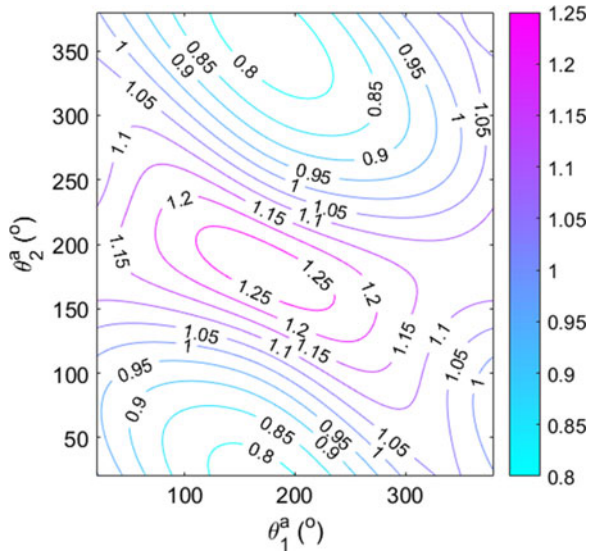

Fig. 9. The contour line varies with the joint angle of Arm-*a* with $m_L = 0$.

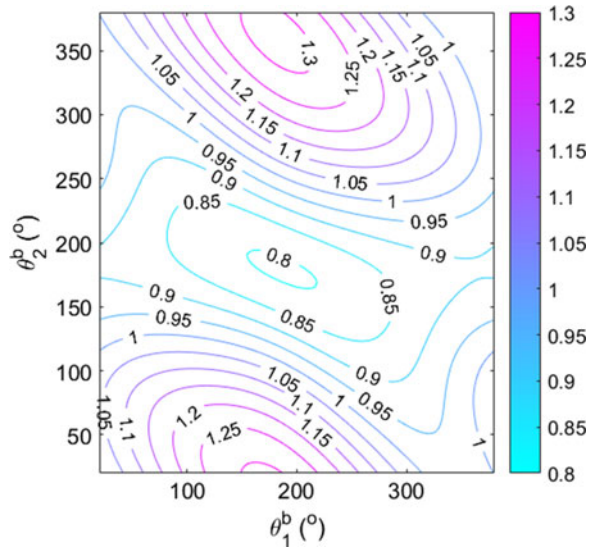

Fig. 10. The contour line varies with the joint angle of Arm-*b* with $m_L = 0$.

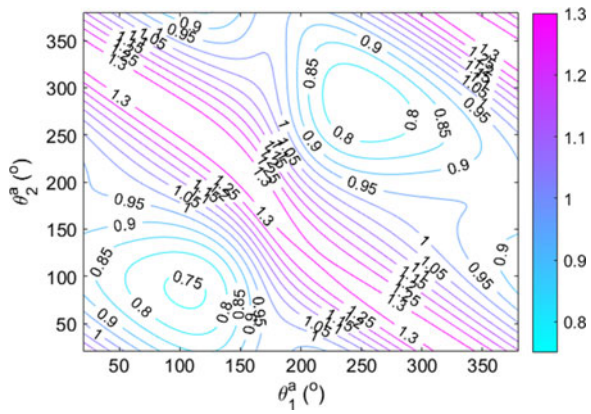

Fig. 11. The contour line varies with the joint angle of Arm-*a* with $m_L = 100$ kg.

https://doi.org/10.1017/S0263574719001826 Published online by Cambridge University Press

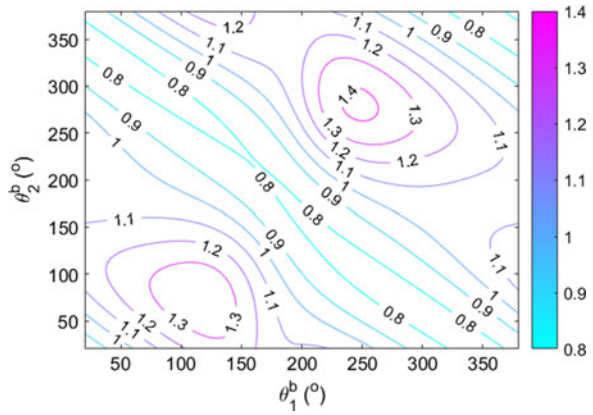

Fig. 12. The contour line varies with the joint angle of Arm-*b* with $m_L = 100$ kg.

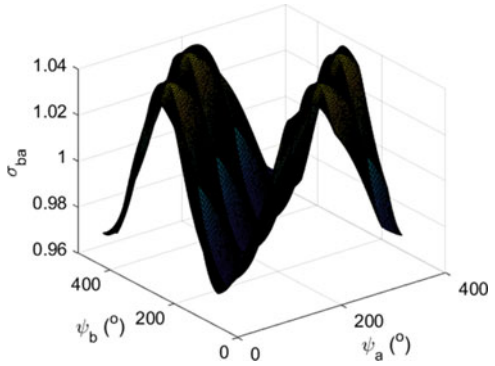

Fig. 13. Coupling factor varies with the installation pose in 3D form.

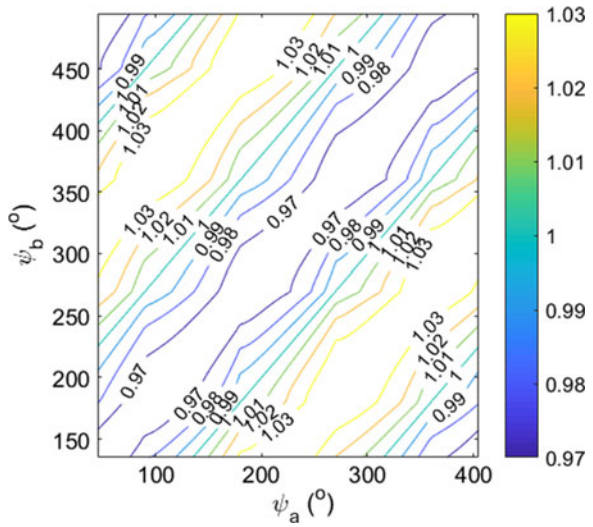

Fig. 14. The contour line varies with the installation pose.

5.1.3. Dynamic coupling between the dual-arm and the base. Similarly, the contour line of the coupling factor of end-to-base that varies with the joint angle of Arm-*a* and Arm-*b* is shown in Figs. 15 and 16, respectively. When the payload of Arm-*a* is $m_L = 100$ kg, the coupling factor that varies with the joint angle of Arm-a and Arm-b is shown in Figs. 17 and 18, respectively.

In addition, the dynamic coupling factor from the dual-arm to the base that varies with the dual-arm installation angle is shown in Fig. 19, and the corresponding contour lines are shown in Fig. 20.

https://doi.org/10.1017/S0263574719001826 Published online by Cambridge University Press

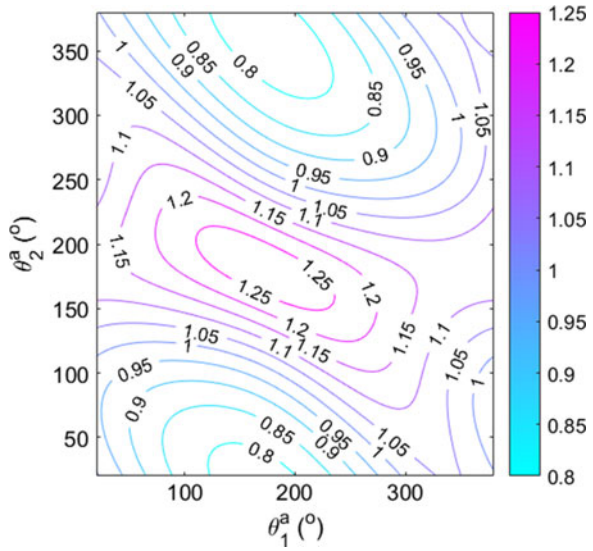

Fig. 15. The contour line varies with the joint angle of Arm-*a* with $m_L = 0$.

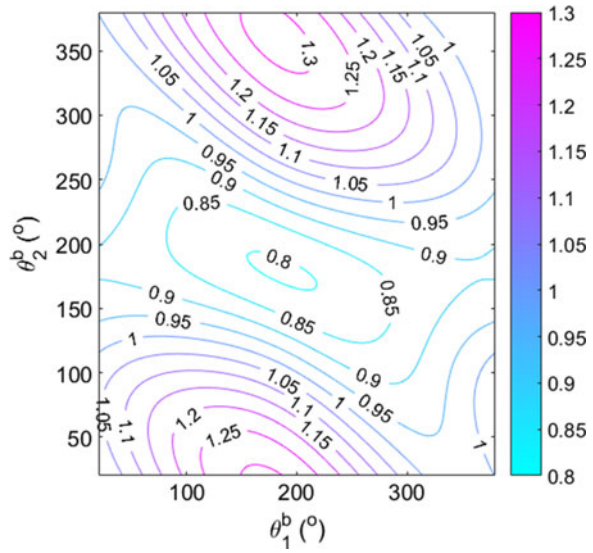

Fig. 16. The contour line varies with the joint angle of Arm-*b* with $m_L = 0$.

5.2. Dynamic coupling application analysis

5.2.1. Multiple coupling effects analysis. From the above analysis, we can get the following properties of the dynamic coupling factor:

(1) If the mass characteristics (i.e. m_i^k and I_i^k) of Arm-*a* are much larger than those of Arm-*b*, that is, the coupling effects from Arm-*a* to Arm-*b* are small, the dynamic coupling is negligible; conversely, the dynamic coupling must be considered.
(2) If the mass characteristics of the base are much larger than those of the two arms, that is, the coupling effects of the two arms to the base are small, the dynamic coupling is negligible; conversely, the dynamic coupling must be considered.
(3) By reasonably designing the installation angle (i.e. φ_k) of the two arms, the distribution of singular matrix can be changed, thereby effectively reducing the dynamic coupling characteristics.
(3) By rationally planning the motion trajectory of the dual-arm space robot, the distribution of the singular matrix can also be changed, thereby effectively reducing the dynamic coupling characteristics.

https://doi.org/10.1017/S0263574719001826 Published online by Cambridge University Press

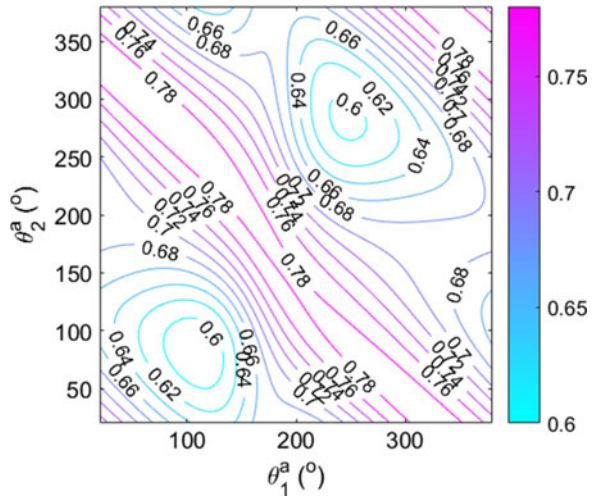

Fig. 17. The contour line varies with Arm-*a* with $m_L = 100$ kg.

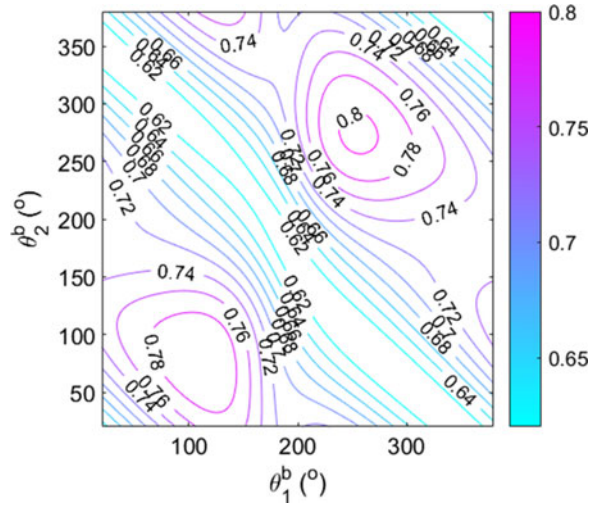

Fig. 18. The contour line varies with Arm-*b* with $m_L = 100$ kg.

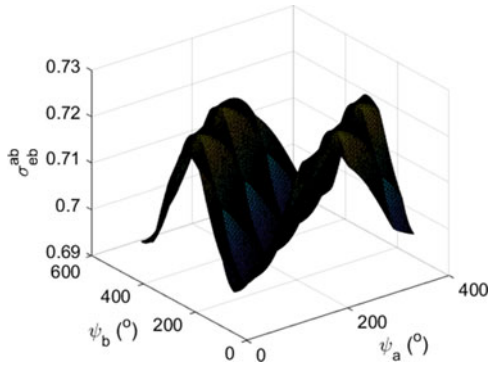

Fig. 19. Coupling factor varies with the installation pose in 3D form.

5.2.2. A 2D case simulation. As shown in Fig. 21, we developed the Matlab/Simulink co-simulation platform,[28] which includes the dual-arm dynamic model, the dual-arm kinematical and dynamic coupling module, the dual-arm controller, and the real-time data display module. The iteration time period of each step of the co-simulation system is $dt = 0.25$ s; the algorithm was controlled by a 64-bit computer, with a 3.7 GHz Core i3-4170 processor and 8 GB ram. As a typical situation,

https://doi.org/10.1017/S0263574719001826 Published online by Cambridge University Press

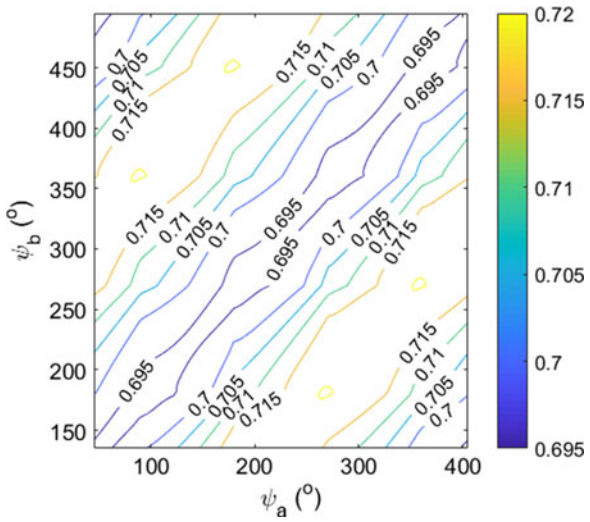

Fig. 20. The contour line varies with the installation pose.

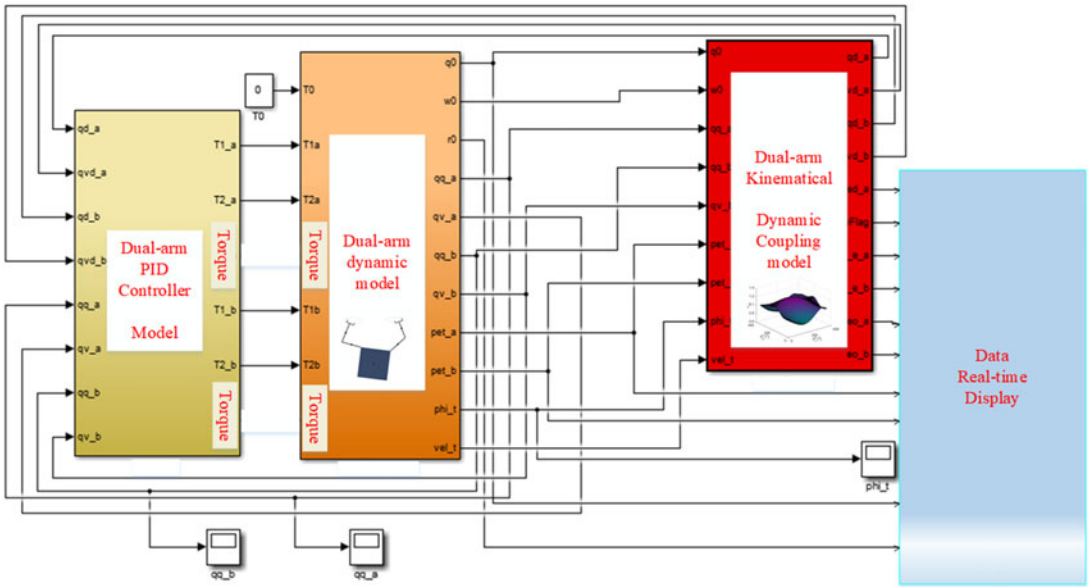

Fig. 21. Matlab/Simulink model of the numerical simulation.

assuming that the payload of Arm-a is $m_{\mathrm{L}} = 100$ kg, the initial joint angles of the dual-arms are $\boldsymbol{\Theta}_a = [-45, 90](^\circ)$, $\boldsymbol{\Theta}_b = [45, -90](^\circ)$, and the initial installation angles of the manipulator are 45° and 135°, respectively.

As shown in Figs. 22 and 23, at the final state, the joint angles of the manipulator are $\boldsymbol{\Theta}_a = [4, 69.5](^\circ)$ and $\boldsymbol{\Theta}_b = [36.7, -97.3]$ (), respectively. In the process of the dual-arm coordinated movement, the traditional point-to-point capture method[29,30] and the base perturbation optimization method based on the dynamic coupling factors between the two arms and the base were used to develop the simulation system, as shown in Fig. 24. The simulation results shown that the dynamic coupling factors between the two arms and the base can be used to reduce the disturbance of the base.

5.2.3. A 3D case simulation. In order to better reflect the advantages of dynamic coupling modeling, here, a 3D simulation model of a dual-arm space robot system is established.[32,33] It is composed of a robot base and two sets of 7-DOF serial manipulators. The model of the dual-arm space robot is shown in Fig. 25. Frames $O_I - X_I Y_I Z_I$, $O_b - X_b Y_b Z_b$, and $O_t^k - X_t^k Y_t^k Z_t^k$ are the inertial system, the base coordinate system, and the target coordinate system, respectively. The symbols $\boldsymbol{P}_t^k$ and $\boldsymbol{\varphi}_t^k$ are the

https://doi.org/10.1017/S0263574719001826 Published online by Cambridge University Press

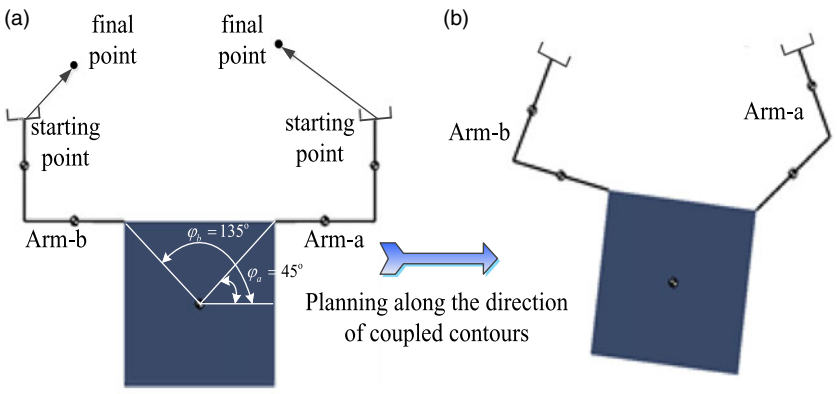

Fig. 22. Matlab/SimMechanical simulation model ((a) and (b) represent the initial and final state of the dual-arm, respectively).

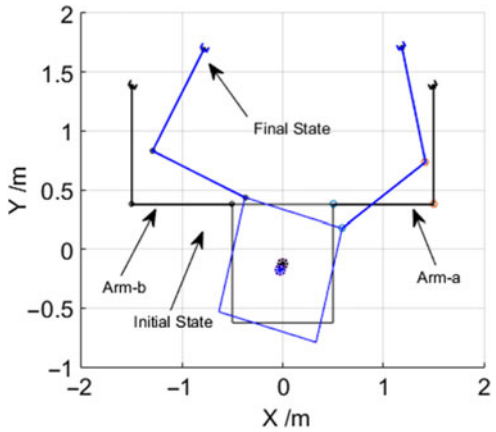

Fig. 23. The schematic diagram of simulation initial state and termination state in 3D coordinate system (the direction perpendicular to the screen is the Z-direction, and $Z = 0$).

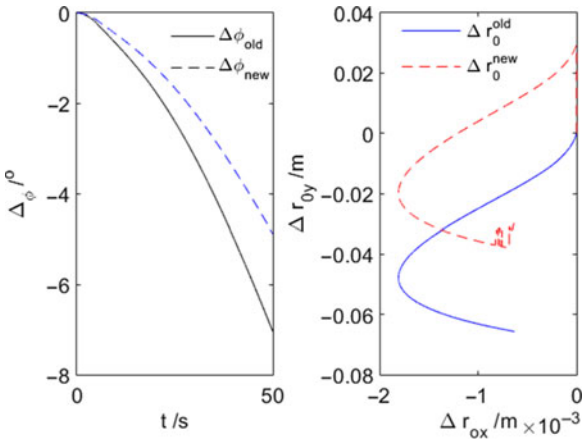

Fig. 24. Disturbance curve of the pose of the base centroid (considering the dynamic coupling).

position vector and rotation transformation matrix from frame $O_I - X_I Y_I Z_I$ to frame $O_t^k - X_t^k Y_t^k Z_t^k$, respectively.

The D-H coordinate systems of the manipulator are shown in Fig. 26. The centroid position, mass, and inertia of each link are listed in Table III.

https://doi.org/10.1017/S0263574719001826 Published online by Cambridge University Press

Table III. The mass properties of the dual-arm space robotic system.

Parameter		**B$_0$**	**B$_1$**	**B$_2$**	**B$_3$**	**B$_4$**	**B$_5$**	**B$_6$**	**B$_7$**
Mass (kg)		2000	11	12	18	10	18	12	11
${}^i\boldsymbol{a}_i$(m)		1.20	0	0	0	0	0	0	0
		0	0	0	0	0	0	0	0
		0	0.10	0	0.90	0.15	0.90	0	0.10
${}^i\boldsymbol{b}_i$(m)		0.90	0	0	0	0	0	0	0
		0	0	0	0	0	0	0	0
		0.75	0.10	0	0.90	0.15	0.90	0	0.10
$\boldsymbol{I}_i$ (kg.m^2)	*Ixx*	800	0.05	0.05	4.89	0.22	4.89	0.06	0.05
	Iyy	600	0.05	0.05	4.89	0.22	4.89	0.06	0.05
	Izz	700	0.03	0.03	0.04	0.03	0.04	0.03	0.03

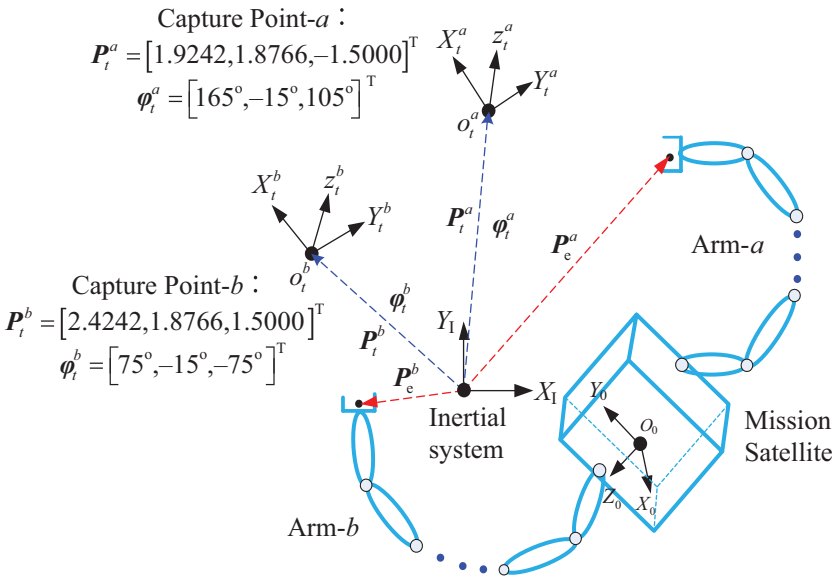

Fig. 25. The diagram of the dual-arm space robot capturing the target.

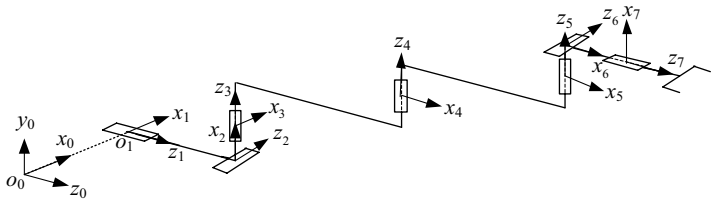

Fig. 26. The D-H coordinate system of the dual-arm space robotic system.

The initial conditions for the simulation are as follows:

(1) Joint angles of Arm-*a* and Arm-*b*:

$$\boldsymbol{\Theta}^b = \boldsymbol{\Theta}^a = [0,\ 45,\ 0,\ -45,\ -90,\ -45,\ 0]^{\mathrm{T}}\ (^{\circ}) \tag{17}$$

(2) The centroid position and attitude of the base are:

$$\boldsymbol{r}_{\mathrm{o}} = [-0.08,\ -0.12,\ 0\ ]^{\mathrm{T}}\ (\mathrm{m}) \tag{18}$$

$$\boldsymbol{\varphi}_{\mathrm{o}} = [0\ \ 0\ \ 0]^{\mathrm{T}} \tag{19}$$

https://doi.org/10.1017/S0263574719001826 Published online by Cambridge University Press

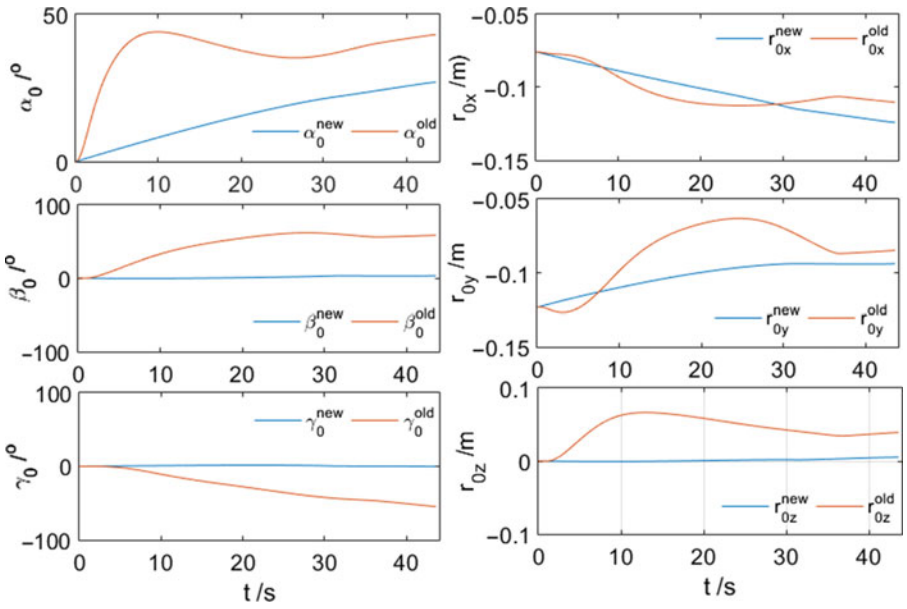

Fig. 27. The deviation of the centroid position and attitude of the base ("old" represents the traditional point-to-point trajectory planning method, "new" represents the new trajectory planning method based on the dynamic coupling factor).

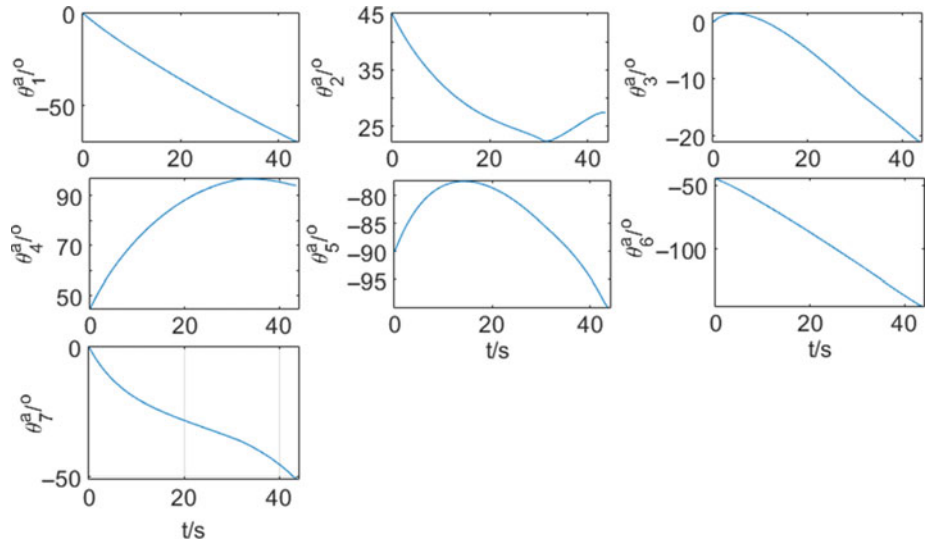

Fig. 28. The curves of the joint angles of Arm-*a*.

The variation curves of the centroid position and attitude of the base are shown in Fig. 27. The simulation results shown that the dynamic coupling factors between the two arms and the base can be used to reduce the disturbance of the base.

The planned trajectories of the joint angles of Arm-*a* and Arm-*b* are shown in Figs. 28 and 29, respectively. The relative pose deviation is shown in Fig. 30. According to the simulation results, the 3D state of the dual-arm space robot corresponding to different times is shown in Fig. 31.

According to the above 2D and 3D simulation results, the disturbance comparison results of the base (including the traditional planning method and the proposed planning method) are shown in Table IV under the same initial conditions.

https://doi.org/10.1017/S0263574719001826 Published online by Cambridge University Press

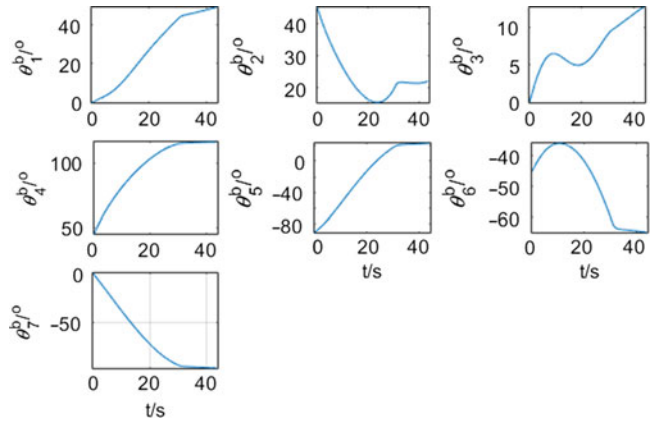

Fig. 29. The curves of the joint angles of Arm-*b*.

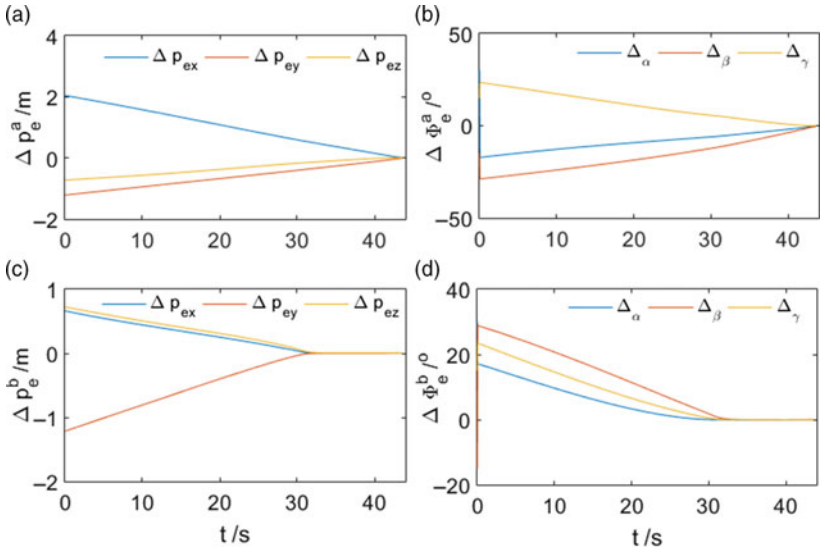

Fig. 30. The relative pose deviation ((a) and (c) represent the relative position deviation of Arm-*a* and Arm-*b*, respectively; (b) and (d) represent the relative attitude deviation of Arm-*a* and Arm-*b*, respectively).

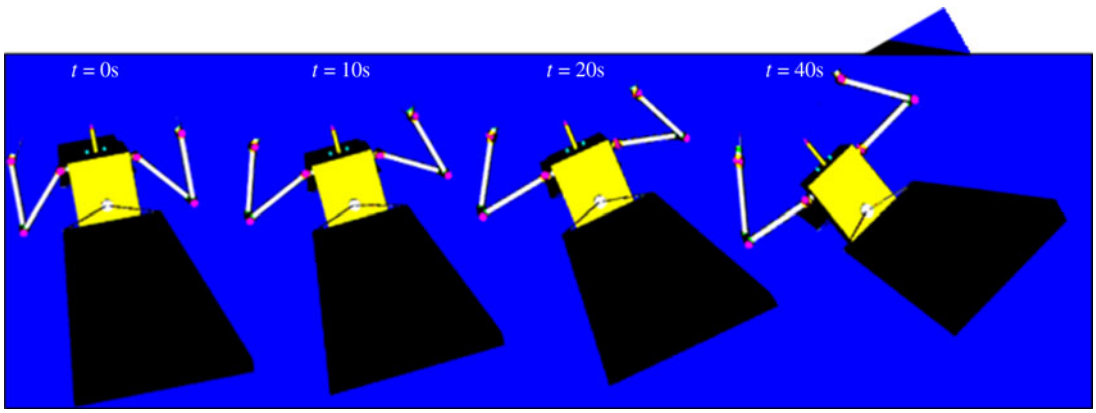

Fig. 31. The 3D state of the dual-arm space robot.

https://doi.org/10.1017/S0263574719001826 Published online by Cambridge University Press

Table IV. Performance comparisons of the two methods.

	Deviation of the centroid position/m		Deviation of the centroid attitude/°	
Parameter	**The old method**	**The new method**	**The old method**	**The new method**
Case: 2D	0.0409	0.0211	7.2113	5.1215
Case: 3D	0.1398	0.1203	90.1388	30.1332

6. Conclusion

In the process of dual-arm cooperative capturing, due to the dynamic coupling between the two arms and between the arm and the base, the trajectory planning and control of the dual-arm coordination become very difficult. In this paper, a dynamic coupling modeling, characteristic analysis, and evaluation method for a dual-arm space robot are proposed. According to the constraints of the angular momentum and the linear momentum of the dual-arm space robot system, the corresponding dynamical coupling equations are deduced, and the dynamic coupling factor is defined to evaluate the multiple dynamic coupling effects. Furthermore, the multiple dynamic coupling effects between two arms and the base are analyzed. The simulation results show the effectiveness of the proposed method. This work is very useful for practical applications; the evaluation function of the capture time and minimizing disturbance of the base are the problems that need to be solved in the future.

In the future, we will further study the dynamic modeling method and the coordination control method of the dual-arm space robot for target post-capturing.

Acknowledgements

This work was supported by the National Natural Science Foundation of China (Grant No. U1613227), Self-Planned Task (No. SKLRS201817B) of State Key Laboratory of Robotics and System (HIT), Guangdong Special Support Program (Grant No.2017TX04X0071), and China Postdoctoral Science Foundation (Grant No. 2019M651274). Thanks to Prof. Han Yuan for his valuable comments on the revision of the paper.

References

1. M. Oda, "Space Robot Experiments on NASDA's ETS-VII Satellite-Preliminary Overview of the Experiment Results," *IEEE International Conference on Robotics and Automation*, Detroit, MI, USA (1999) pp. 1390–1395.
2. M. Shan, J. Guo and E. Gill, "Review and comparison of active space debris capturing and removal methods," *Prog. Aerosp Sci.* **80**, 18–32 (2016).
3. A. Flores-Abad, O. Ma, K. Pham and S. Ulrich, "A review of space robotics technologies for on-orbit servicing," *Prog. Aerosp. Sci.* **68**, 1–26 (2014).
4. D. Nenchev, Y. Umetani and K. Yoshida, "Analysis of a redundant free-flying spacecraft/manipulator system," *IEEE Trans. Rob. Autom.* **8**(1), 1–6 (1992).
5. P. Huang, F. Zhang, Z. Meng and Z. Liu, "Adaptive control for space debris removal with uncertain kinematics, dynamics and states," *Acta Astronaut.* **128**(11–12), 416–430 (2016).
6. E. Coleshill, L. Oshinowo, R. Rembala, B. Bina, D. Rey and S. Sindelar, "Dextre: Improving maintenance operations on the International Space Station," *Acta Astronaut.* **64**(9), 869–874 (2009).
7. P. Huang, F. Zhang, J. Cai, D. Wang, Z. Meng and J. Guo, "Dexterous tethered space robot: Design, measurement, control and experiment," *IEEE Trans. Aerosp. Electron. Syst.* **53**(3), 1452–1468 (2017).
8. F. Zhang and P. Huang, "Releasing dynamics and stability control of maneuverable tethered space net," *IEEE/ASME Trans. Mechatron.* **22**(2), 983–993 (2017).
9. K. Nanos and E. Papadopoulos, "On Cartesian Motions with Singularities Avoidance for Free-Floating Space Robots," *2012 IEEE International Conference on Robotics and Automation*, Saint Paul, MN, USA (2012) vol. 20, pp. 5398–5403.
10. K. Nanos and E. Papadopoulos, "Avoiding dynamic singularities in Cartesian motions of free-floating manipulators," *IEEE Trans. Aerosp. Electron. Syst.* **51**(3), 2305–2318 (2015).
11. Y. Xu, H.Y. Shum, T. Kanade and J. Lee, "Parameterization and adaptive control of space robot systems," *IEEE Trans. Aerosp. Electron. Syst.* **30**(2), 435–451 (1994).
12. H. Wang and Y. Xie, "Prediction error based adaptive Jacobian tracking for free-floating space manipulators," *IEEE Trans. Aerosp. Electron. Syst.* **48**(4), 3207–3221 (2012).
13. W. Xu, C. Li, X. Wang, B. Liang, Y. Liu and Y. Xu, "Study on non-holonomic cartesian path planning of free-floating space robotic system," *Adv. Rob.* **23**(1–2), 113–143 (2009).
14. W. Xu, Y. Liu, B. Liang, X. Wang and Y. Xu, "Unified multi-domain modeling and simulation of space robot for capturing a moving target," *Multibody Syst. Dyn.* **23**(3), 293–331 (2010).

https://doi.org/10.1017/S0263574719001826 Published online by Cambridge University Press

15. Y. Xu and H. Shum, "Dynamic control and coupling of a free-flying space robot system," *J. Rob. Syst.* **11**(7), 573–589 (1994).
16. M. Bergerman, C. Lee and Y. Xu, "Dynamic Coupling of Underactuated Manipulators," *4th IEEE Conference on Control Applications*, Albany, NY, USA (1995) pp. 500–505.
17. S. Ali, A. Moosavian and E. Papadopoulos, "On the kinematics of multiple manipulator space free-flyers and their computation," *J. Rob. Syst.* **15**(4), 1–19 (1998).
18. E. Papadopoulos, S. Ali and A. Moosavian, "Dynamics and control of space free-flyers with multiple manipulators," *Adv. Rob.* **9**(6), 603–624 (1994).
19. S. Ali, A. Moosavian and E. Papadopoulos, "Explicit dynamics of space free-flyers with multiple manipulators via SPACEMAPLE," *Adv. Rob.* **18**(2), 223–244 (2004).
20. A. A. Hafez, V. V. Anurag, S. V. Shah, K. M. Krishna and C. V. Jawahar, "Reactionless visual servoing of a dual-arm space robot," *IEEE International Conference on Robotics and Automation*, Hong Kong, China (2014) pp. 4475–4480.
21. A. A. Hafez, P. Mithun, V. Anurag, S. Shah and K. M. Krishna, "Reactionless visual servoing of a multi-arm space robot combined with other manipulation tasks," *Rob. Auton. Syst.* **91**, 1–10 (2016).
22. M. Wang, J. Luo, J. Yuan and U. Walter, "Coordinated trajectory planning of dual-arm space robot using constrained particle swarm optimization," *Acta Astron.* **146**, 259–272 (2018).
23. J. Peng, W. Xu, E. Pan, L. Yan, B. Liang and A. Wu, "Dual-arm coordinated capturing of an unknown tumbling target based on efficient parameters estimation," *Acta Astron.* **162**, 589–607 (2019).
24. S. V. Shah, I. Sharf and A. K. Misra, "Reactionless Path Planning Strategies for Capture of Tumbling Objects in Space Using a Dual-Arm Robotic System," *AIAA Guidance, Navigation & Control*, Boston, MA, USA (2013) pp. 1–8.
25. P. Huang, Y. Xu and B. Liang, "Dynamic balance control of multi-arm free-floating space robots," *Int. J. Adv. Rob. Syst.* **2**(2), 398–403 (2006).
26. Z. Vafa and S. Dubowsky, "The kinematics and dynamics of space manipulators: The virtual manipulator approach," *Int. J. Rob. Res.* **9**(4), 3–21 (1990).
27. W. Xu, J. Peng, B. Liang and Z. Mu, "Hybrid modeling and analysis method for dynamic coupling of space robots," *IEEE Trans. Aerosp. Electron. Syst.* **52**(1), 85–98 (2016).
28. J. Peng, W. Xu, Z. Wang and Y. She, "Dynamic Analysis of the Compounded System Formed by Dual-arm Space Robot and the Captured Target," *International Conference on Robotics and Biomimetics*, Shenzhen, China (2013) pp. 1532–1537.
29. W. Xu, Y. Liu and Y. Xu, "The coordinated motion planning of a dual-arm space robot for target capturing," *Robotica* **30**(5), 755–771 (2012).
30. W. Xu, B. Liang, C. Li and Y. Xu, "Autonomous rendezvous and robotic capturing of non-cooperative target in space," *Robotica* **28**(5), 705–718 (2010).
31. W. Xu, B. Liang, C. Li, Y. Liu and Y. Xu, "Autonomous target capturing of free-floating space robot: Theory and experiments," *Robotica* **27**(2), 425–445 (2009).
32. J. Peng, W. Xu, B. Liang and A. Wu, "Virtual stereo-vision measurement of non-cooperative space targets for a dual-arm space robot," *IEEE Trans. Instrum. Meas.* **69**(1), 1–13 (2019).
33. W. Xu, D. Meng, H. Liu, X. Wang and B. Liang, "Singularity-free trajectory planning of free-floating multiarm space robots for keeping the base inertially stabilized," *IEEE Trans. Syst. Man Cybern. Syst.* **49**(12), 1–13 (2017).